Properties of low-lying states in ^{142}Ce via high resolution electron scattering

W. Kim, J. R. Calarco, J. P. Connelly,* J. H. Heisenberg, F. W. Hersman, T. E. Milliman, and J. E. Wise†
Department of Physics, University of New Hampshire, Durham, New Hampshire 03824

B. L. Miller and C. N. Papanicolas
Department of Physics and Nuclear Physics Laboratory, University of Illinois at Urbana-Champaign, 1110 West Green Street, Urbana, Illinois 61801

V. Yu. Ponomarev
Laboratory of Theoretical Physics, Joint Institute for Nuclear Research, Dubna, Head Post Office P. O. Box 79, SU-101000 Moscow, U.S.S.R.

E. E. Saperstein and A. P. Platonov
I. V. Kurchatov Institute of Atomic Energy, Moscow 123182, U.S.S.R.
(Received 8 May 1991)

Differential cross sections for inelastic scattering from ^{142}Ce have been measured for excitation energies less than 3.3 MeV over a range of momentum transfer of 0.4 to 2.5 fm^{-1}. The data have been analyzed to extract transition charge densities. These densities are interpreted in terms of a quasiparticle-phonon approach and finite Fermi system theory to disentangle the collective and noncollective modes of excitation.

I. INTRODUCTION

Electron scattering is well suited for examining the spatial properties of nuclear wave functions due to the purely electromagnetic character of the reaction mechanism and the well-understood relationship between the measured cross section and the nuclear charge and current densities. The charge and transition charge densities of the nucleus provide the meeting ground theory and experiment. Shape differences in these densities make it possible to discriminate between collective and noncollective modes of excitation for transitions of the same multipolarity.

Early experiments [1] on inelastic electron scattering from magic nuclei were instrumental in revealing the surface nature of the low-lying collective states of natural parity. Such behavior was predicted by structure calculations employing both the Hartree-Fock (HF) approach with effective forces [2], and the finite Fermi systems (FFS) theory using the coordinate representation technique for calculation of the nuclear response function [3–5].

There are several electron scattering measurements presently available for the energetically lowest 2^+ states in semimagic and nonmagic spherical nuclei. Measurements on the even-even Zn isotopes have been made [6], and calculations carried out [7], using the same technique as for magic nuclei but slightly modified for the case of partially occupied levels. It has been reported that the transition charge densities to the lowest two-neutron-quasiparticle excitations in ^{204}Pb and ^{206}Pb exhibit a remarkable similarity to the lowest collective excitation of the ^{208}Pb. It is suggested in that paper that these collective excitations act as an important doorway in the dressing of the lowest two-neutron-quasiparticle configurations by an effective charge, and their proper description and inclusion in any core-polarization calculation appears essential in achieving agreement between theory and experiment. Efforts have been made to disentangle the contributions of collective and noncollective modes of excitation for transitions of the same multipolarity in the $N=50$ region. A comparison of low-lying quadrupole excitations in ^{88}Sr, ^{89}Y, and ^{90}Zr established [9] the strong single-particle nature of these states which had previously been thought to be collective vibrations.

Recently, the nuclei in the rare-earth mass region have been extensively studied by electron scattering with high resolution. Charge and transition charge densities for the ground-state rotational band (0^+, 2^+, 4^+, and 6^+) of ^{152}Sm were extracted from electron scattering cross sections and compared with Hartree-Fock-Bogoliuov calculations [10]. Transition charge densities for the first excited 2^+ state in five samarium isotopes (144, 148, 150, 152, and 154) were obtained and studied in terms of the interacting boson model [11]. The low-lying quadrupole states in ^{142}Nd have been investigated by inelastic electron scattering [12,13], and it has been found that the extracted transition charge densities indicate quite different microscopic structure for these states. On the basis of a quasiparticle-phonon approach, it has been shown that this difference can be understood as arising from an interplay between collective and single-particle excitation modes.

We present here the results of a high resolution elec-

tron scattering experiment in which cross sections have been obtained for the ground state and low-lying excited states in ^{142}Ce. In this mass region, low-lying excitations for odd-even nuclides exhibit excitations with a large single-particle component, while for the even-even nuclides such as ^{142}Ce the lowest-lying transitions show strong collectivity and significant pairing. To interpret experimental transition charge densities, calculations employing two theoretical approaches have been performed. The first is the quasiparticle-phonon approach (QPA) [14–17], which has been successfully applied to the description of the transition charge densities of the low-lying 2^+ states in ^{142}Nd [12]. The second one is the finite Fermi system (FFS) Theory [18] within which the shapes of the transition charge densities for the first 2^+ states have been predicted for a wide range of isotopes.

II. EXPERIMENTAL PROCEDURE

The data for this experiment were collected using the energy-loss spectrometer system (ELSSY) at the MIT–Bates Linear Accelerator Center consisting of a 900-MeV/c energy-loss spectrometer [19], with a nominal solid angle of 3.3 msr and a momentum bite of $\pm 3\%$. The beam energy was varied in the range of 100–370 MeV. Average currents of 25–35 μA were used. Beam current was measured to one part in 10^3 using the signals from two toroids fed into integrating amplifiers.

The scattering angle ranged from 40° to 101°, corresponding to a range of effective momentum transfer q_{eff} between 0.4 and 2.5 fm^{-1}, where $q_{\text{eff}}=q(1+3Ze^2/2ER)$ and R is the nuclear RMS radius. One additional measurement was performed at 155° and at a beam energy of 190 MeV ($q_{\text{eff}}=2.0$ fm^{-1}) to investigate the transverse contribution to the form factor. The transverse contributions to the form factor at forward angles are expected to be negligible. The upper limits of the ratio in $|F^T/F^C|^2$, where F^T and F^C are transverse and longitudinal form factors, respectively, were observed to be 0.8% for the 2_1^+ state ($E_x=0.641$ MeV), 0.7% for the 3_1^- state ($E_x=1.653$ MeV), and 0.8% for the 4_1^+ state ($E_x=1.219$ MeV). The ratios for other excited states were 9% for the 3_2^- state ($E_x=3.060$ MeV) and 5% for the 4_2^+ state ($E_x=2.043$ MeV). This result is also confirmed by the recent NIKHEF electron scattering results [12,13] on ^{142}Nd. At the forward angles corresponding to the first minimum of longitudinal form factor ($q_{\text{eff}}=1.0$ fm^{-1}), the transverse components of the cross section for the quadrupole states of ^{142}Nd were measured to be less than 2% of the longitudinal form factor. Calculations with QPA have shown that the transverse form factors of all the quadrupole states reach their maximum value near the minimum of the charge form factor. For the states of other multipolarities in ^{142}Nd, QPA calculations [13] predict the transverse contribution to be of the same order as for the quadrupole states. We will therefore neglect the small transverse components of the natural parity ^{142}Ce states in the analysis.

As part of the current experiment, effort was devoted to a continuing program of energy resolution enhancement, primarily through studies of beam tuning systematics and data acquisition software refinement. This program resulted in attaining ultimate resolutions of $\Delta p/p=4\times10^{-5}$ and routinely gave 6×10^{-5}. This was essential for studying an excitation region with such a high density of states.

The focal plane instrumentation consists of two vertical drift chambers, the first of which is positioned approximately at the focal surface, two transverse arrays connected in series, two Čerenkov detectors, and the associated readout electronics [20]. The instrumentation is located outside of the spectrometer vacuum and is separated from the spectrometer vacuum by a thin Kevlar-reinforced Mylar window [21].

This experiment used ^{142}Ce targets with thickness of 4.92 and 20.19 mg/cm^2, isotopically enriched to 92.11%. Most of the impurity is ^{140}Ce (7.89%). Additional data were taken on either BeO or BeAl, ^{12}C, and ^{140}Ce to establish focal plane parameters and energy calibrations using excited states and differential recoil from the various nulcides and to measure background. The ^{12}C targets were also used to establish normalizations.

III. DATA REDUCTION

A. Extraction of cross sections

Cross sections were extracted from the experimental spectra using the line-shape fitting code ALLFIT [22]. A typical experimental spectrum and the associated line shape is shown in Fig. 1. The peak integrals extracted from the spectra were corrected for straggling, bremsstrahlung, and Schwinger radiative effects according to the prescription of Bergstrom [23]. In addition, on-line diagnostic spectra were accumulated so that corrections could be applied to compensate for the misidentification of good events and instrumental dead time. For the forward angle data, these corrections were normally of the order of a few percent and were dominated by the dead-time correction. At backward angles, where the counting rate is low, instrumental dead time is negligible and the correction is dominated by good event corrupted by spurious background events. All the data were also corrected for folding over the spectrometer acceptance and for multiple scattering in the target.

Due to possible uncertainties in the effective target thickness, in the incident electron energy, and in the corrections applied to compensate for hardware head time and software rejection of corrupted good events, it was necessary to normalize each data set. Angular distributions of the elastic form factor were obtained from the measurements with four different beam energies. A normalization was obtained for each incident energy using a best fit of the measured elastic cross sections and the Barrett moments obtained from results of muonic x-ray experiments [24]. The normalization factors ranged from 0.81 to 1.08. The inelastic scattering cross sections measured were corrected using the same normalization factor that was obtained from the fit to the elastic scattering data.

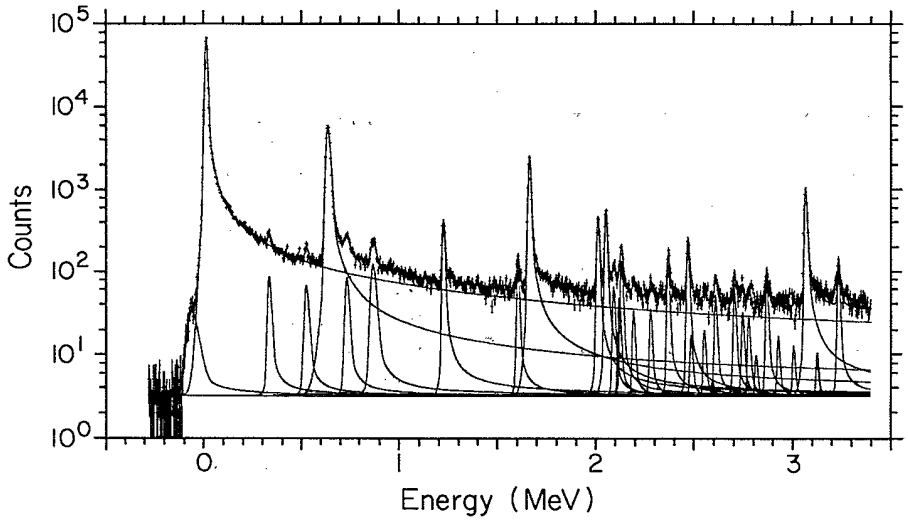

FIG. 1. Spectrum and line-shape fit of 190-MeV electron scattered from ^{142}Ce at 45°.

B. Transition charge densities

Cross sections extracted from the electron scattering spectra were fit using distorted-wave Born approximation (DWBA) phase-shift code [25]. A polynomial-Gaussian (PG) model for transition densities was used to extract structure information from the experimental cross sections. In the PG model the density is expressed as

$$\rho(r)=\sum_{n=1}^{5} A_n (r/r_0)^{2n+l} e^{-(r/r_0)^2} . \quad (1)$$

This expansion produces terms which fall off like e^{-r^2} at large r which is the same behavior as for harmonic-oscillator wave functions. Up to five terms are used in the polynomial and the radius parameter r_0 can be fit. Fast convergence properties of this expansion allow excellent fits and provide a reasonable method for the reconstruction of nuclear transition densities.

IV. THEORETICAL DESCRIPTION OF LOW-LYING NUCLEAR EXCITATIONS

In this section we briefly outline the two theoretical models we have used here for interpreting the experimental data, the QPA and FFS theories. Both approaches have many common features since both are microscopic theories starting from the quasiparticle basis. They differ in the form of the quasiparticle interaction and in some essential details. The FFS theory employs a realistic form of the residual interaction between quasiparticles with a single fixed set of parameters for different nuclei. On the other hand, this theory does not treat in detail the interplay between modes of excitation. This interplay is consistently taken into account within the QPA, but this approach deals with the more schematic form of the residual interaction with parameters adjusted to the experimental data for each nucleus.

A. Quasiparticle-phonon approach

In the quasiparticle-phonon approach (QPA) [14–17] excited states in even-even nuclei are considered as a combination of one-, two-, . . . , phonon states built on the ground-state wave function $\Psi_{\text{g.s.}}$ which is treated as a phonon vacuum. Thus, the wave function of the state with momentum J and projection M has the form

$$\Psi_\nu(JM)=\left\{\sum_i R_i(J\nu)Q^\dagger_{JMi}+\sum_{LiL'i'} P^{L'i'}_{Li}(J\nu)[Q^\dagger_{L\mu i}Q^\dagger_{L'\mu'i'}]_{JM} + \sum_{LiL'i'}\sum_{J'L''i''} T^{J'L''i''}_{LiL'i'}(J\nu)[[Q^\dagger_{L\mu i}Q^\dagger_{L'\mu'i'}]_{J'M'}Q^\dagger_{L''\mu''i''}]_{JM}+\cdots\right\}\Psi_{\text{g.s.}} \quad (2)$$

with the definition

$$[Q^\dagger_{L\mu i}Q^\dagger_{L'\mu'i'}]_{JM}\equiv\sum_{\mu\mu'}\langle L\mu L'\mu'|JM\rangle Q^\dagger_{L\mu i}Q^\dagger_{L'\mu'i'} , \quad (3)$$

where $Q^\dagger_{L\mu i}$ is the phonon creation operator with angular momentum L, projection μ, and the RPA root number i. Phonons are constructed as a linear combination of pairs of quasiparticle creation $\alpha^\dagger_{jm}$ and annihilation α_{jm} operators with the shell quantum numbers $jm\equiv|n,l,j,m\rangle$ as follows:

$$Q^{\dagger}_{L\mu i}=\frac{1}{2}\sum_{jj'}^{N,Z}\{\psi^{Li}_{jj'}[\alpha^{\dagger}_{jm}\alpha^{\dagger}_{j'm'}]_{L\mu} +(-1)^{L-\mu}\phi^{Li}_{jj'}[\alpha_{jm}\alpha_{j'm'}]_{L-\mu}\} . \quad (4)$$

To obtain the phonon basis (i.e., excitation energies ω_{Li} and structure coefficients $\psi^{Li}_{jj'}$ and $\phi^{Li}_{jj'}$), we solve the RPA equations for each J^{π} with the effective Hamiltonian

$$H=H_{\text{s.p.}}+H_{\text{pair}}+H_{\text{res.int.}} , \quad (5)$$

where the first term describes the motion of independent nucleons in the self-consistent average field $U(r)$, the second term represents the pairing interaction, and the last term is the effective residual interaction between quasiparticles. $H_{\text{res.int.}}$ is considered in QPA in separable form, with the factor factor of the residual interaction taken as $\partial U(r)/\partial r$. It is possible to show that for the collective vibrations, this form factor gives a form close to the residual interaction used in the FFS theory. Among the phonon excitations there are both collective phonons such as $Q^{\dagger}_{2^+_1}\equiv Q^{\dagger}_{2\mu 1}$ or $Q^{\dagger}_{3^-_1}$ phonons, and noncollective phonons, even practically pure two-quasiparticle modes. With the obtained phonon basis, Hamiltonian (5) can be rewritten in terms of phonon operators,

$$H=\sum_{L\mu i}\omega_{Li}Q^{\dagger}_{L\mu i}Q_{L\mu i} +\frac{1}{2\sqrt{2}}\sum_{L\mu i}\sum_{L'i'L''i''}\{\overline{U}^{L''i''}_{L'i'}(Li)[Q^{\dagger}_{L'\mu'i'}Q^{\dagger}_{L''\mu''i''}]_{L\mu}Q_{L\mu i} +\text{H.c.}\} . \quad (6)$$

The first term in Eq. (6) corresponds to the noninteracting phonon approximation. The second one describes the interaction between different parts of the wave function in Eq. (2) with the exchange of one phonon. The explicit expression for the matrix element $\overline{U}^{L''i''}_{L'i'}(Li)$ of the interaction between one- and two-phonon components of the wave function in Eq. (2), in terms of the phonon amplitudes $\psi^{Li}_{jj'}$, $\phi^{Li}_{jj'}$ and matrix elements of the residual interaction, can be found in Refs. [16] and [26], and they are calculated by computer code GIRES [26]. Once the phonon basis is introduced there are no free parameters for the description of the phonon modes interaction.

In this paper we truncate the wave function of the excited states in Eq. (2), including only terms up to the three-phonon term. After diagonalization of the Hamiltonian in Eq. (6) we obtain the energies of the states ηJ_{ν} (ν is the root number) and structure coefficients R, P, and T. Since the phonon operators are not ideal bosons, the commutation relations must take into account their fermion structure in order not to violate the Pauli principle. In our approach, the Pauli principle is taken into account in the diagonal approximation, which is both sufficient for this kind of calculation and simplifies the calculation. (For additional details, see Refs. [12,16,17,26,27].)

The wave function of the ground state $\Psi_{\text{g.s.}}$ is treated as a phonon vacuum. This is correct if we are dealing with noninteracting phonons. However, if we take into account the interaction between them, ground-state correlations appear. To estimate the role of the ground-state correlations we have performed a so-called second-RPA calculation, in which these correlations are accurately taken into account, with the wave function of excited states including only one- and two-phonon terms. We have found that in the case of ^{142}Ce the role of these correlations is negligibly small and they are not included in the following calculations.

If the ground-state correlations are neglected, only one-phonon transition density $\rho^{J}_{i}(r)$ and two-phonon transition densities $\rho^{J}_{LiL'i'}(r)$ contribute to the densities $\rho^{J}_{\nu}(r)$ of the excited states in Eq. (2):

$$\rho^{J}_{\nu}(R)=\sum_{i}R_i(J\nu)\rho^{J}_{i}(r)+\sum_{LiL'i'}P^{L'i'}_{Li}(J\nu)\rho^{J}_{LiL'i'}(r) , \quad (7)$$

where

$$\rho^{J}_{i}(R)=\sum_{jj'}^{N,Z}\rho^{J}_{jj'}(r)\frac{u^{(+)}_{jj'}}{2}(\psi^{Ji}_{jj'}+\phi^{Ji}_{jj'}) , \quad (8)$$

$$\rho^{J}_{LiL'i'}(r)=-\sum_{jj'j''}^{N,Z}\sum_{LiL'i'}\rho^{J}_{jj'}(r)v^{(-)}_{jj''}\hat{L}\hat{L}'\begin{Bmatrix}L & L' & J\\ j & j' & j''\end{Bmatrix}(\psi^{Li}_{j'j''}\phi^{L'i'}_{j''j}+\phi^{Li}_{j'j''}\psi^{L'i'}_{j''j}),\quad \hat{L}=\sqrt{2L+1} . \quad (9)$$

The two-quasiparticle charge transition densities $\rho^{J}_{jj'}(r)$ have a well-known form [29]

$$\rho^{J}_{jj'}(r)=(-1)^{j-1/2}i^{l'-l-J}\frac{\hat{j}\hat{j}'}{\hat{J}4\sqrt{\pi}}[1+(-1)^{l+l'+J}]e_{\tau}\langle j\tfrac{1}{2}j'-\tfrac{1}{2}|J0\rangle R^{*}_{j}(r)R_{j'}(r) , \quad (10)$$

where $u^{(+)}_{jj'}=u_jv_{j'}+u_{j'}v_j$ and $v^{(-)}_{jj'}=u_ju_{j'}-v_{j'}v_j$ are combinations of the coefficients u_j,v_j of the Bogoliubov transformation. $R_j(r)$ is the radial part of the single-particle wave function and e_{τ} is the nucleon effective charge. In the present calculations, the effective charges used are $e_Z=N/A$, $e_N=-Z/A$ for $J^{\pi}=1^-$, and $e_Z=1$, $e_N=0$ for the other J^{π}. The calculated transition charge densities $\rho^{J}_{\nu}(r)$ have been folded with the form factor of the proton charge distribution [29].

For the singe-particle part of the Hamiltonian in Eq. (5), we use the Woods-Saxon potential with the parameters of Lanen [30] for protons and Ponomarev *et al.* [31] for neutrons. The bound states and the narrow quasi-bound states in continuum with the width of a few keV

are included in the calculations; 28 level for neutrons and 29 levels for protons with $j \leq 9$. With this single-particle spectrum, the model-independent energy-weighted sum rule for $J^\pi \leq 4^+$ is well reproduced. Pairing correlations are treated in the BCS approximation with the monopole pairing interaction in the particle-particle channel. A constant matrix element is chosen to reproduce the odd-even mass difference of neighboring isotones. For the $H_{\text{res.int.}}$ part of the Hamiltonian we use a separable multipole interaction in the particle-hole channel with a form factor of the residual forces as a derivative of the central part of the Woods-Saxon potential. The parameters of the effective residual forces are chosen to reproduce the experimental energies and the $B(E\lambda)$ values of the lowest state for each J^π. The strength ratio for the isovector to the isoscalar forces is set at $\kappa_1^{J^\pi}/\kappa_0^{J^\pi} = -1.2$ and the difference in the obtained absolute values $\kappa_{0,1}^{J^\pi}$ for different J^π is only a few percent. The wave function in Eq. (2) was truncated to include all one-phonon states (even very weak) with the excitation energy $E_x \leq 4$ MeV; two-phonon states with $E_x \leq 6$ MeV constructed of phonons with $L^\pi = 1^-, 2^+, 3^-, 4^+, 5^-$, and 6^+; and three-phonon states constructed of the low-lying collective phonons. The calculations for the 2_1^+ state with the enlarged phonon basis was tested and confirms that the truncated configurations did not strongly affect our results on the low-lying states.

B. Finite Fermi system theory

The finite Fermi system (FFS) theory treats the interaction between single-particle and collective modes as well as between different collective modes without introducing any additional parameters. Up until now such an approach was realized only for the case of weak interactions between these modes. In the case the "one-phonon" approximation is a reasonable first step and the anharmonic corrections may be taken into account via the perturbation theory [32]. We review here briefly the FFS theory of description of one-phonon states.

The coordinate (r) representation of the particle-hole propagator [33,34] has been used previously for the case of magic (nonsuperfluid) nuclei [5,35]. This technique makes it possible to avoid any truncation of the shell-model (λ) basis, which proves to be very important for describing the collective low-lying natural parity states which are essentially surface vibrations. The reason for this is that the corresponding transition densities have a form close to the one given by the Bohr-Mottelson collective model $\rho_{\text{BM}}^J \sim d\rho_0/dr$, where ρ_0 stands for the ground-state charge density. Therefore in the λ representation the sum

$$\rho^J(\mathbf{r}) = \sum_{\lambda\lambda'} \rho^J_{\lambda\lambda'} \phi^*_\lambda(\mathbf{r}) \phi_{\lambda'}(\mathbf{r}) \tag{11}$$

contains a large number of components contributing in a coherent way in the surface region. Here, ϕ_λ stands for the single-particle wave functions with corresponding energies ε_λ. Any truncations of the λ basis may lead to errors which must be carefully controlled.

For nonmagic nuclei the pairing correlations effects should be taken into account. In Ref. [18] this was carried out employing the mixed (r,λ) representation technique. Here we sketch only the main ideas of this method. For simplicity, we examine the case of nonsuperfluid nuclei. In the FFS theory, the main equations are obtained using the Green-function technique. Within the one-phonon approximations, the relation density may be found by solving the RPA-like integral equation which has the form

$$\rho_s^J(\mathbf{r}) = \int \mathcal{A}(\mathbf{r}_1,\mathbf{r}_2,E_s^J)\mathcal{F}(\mathbf{r}_1,\mathbf{r}_2)\rho_s^J(\mathbf{r}_2)d\mathbf{r}_1 d\mathbf{r}_2 \,. \tag{12}$$

Here $\mathcal{F}$ is the effective quasiparticle interaction and $\mathcal{A}$ stands for the particle-hole propagator given by the energy integral of the product of two Green functions:

$$\mathcal{A}(\mathbf{r}_1,\mathbf{r}_2,E) = \int \frac{d\varepsilon}{2\pi i} G(\mathbf{r}_1,\mathbf{r}_2,\varepsilon+E)G(\mathbf{r}_2,\mathbf{r}_1,\varepsilon) \,. \tag{13}$$

Solving Eq. (12) for each multipolarity J we obtain the set of one-phonon excited states with excitation energies E_s^J and transition densities $\rho_s^J(\mathbf{r})$.

The Green function can be written in the multipole expansion form

$$G(\mathbf{r}_1,\mathbf{r}_2,\varepsilon) = \sum_\lambda \varphi^*_\lambda(\mathbf{r}_1)\varphi_\lambda(\mathbf{r}_2)/[\varepsilon-\varepsilon_\lambda+i\delta\theta(\varepsilon_\lambda-\mu)] \,, \tag{14}$$

where μ is the Fermi energy and $\delta \to 0$. Substituting one of the Green functions in Eq. (13) by Eq. (14) we obtain the finite sum

$$\mathcal{A}(\mathbf{r}_1,\mathbf{r}_2,E) = \sum_\lambda n_\lambda \varphi^*_\lambda(\mathbf{r}_1)\varphi_\lambda(\mathbf{r}_2)[G(\mathbf{r}_1,\mathbf{r}_2,\varepsilon_\lambda+E) + G(\mathbf{r}_1,\mathbf{r}_2,\varepsilon_\lambda-E)] \,, \tag{15}$$

where the occupation numbers are given by

$$n_\lambda = \begin{cases} 1, & \text{if } \varepsilon_\lambda < \mu \\ 0, & \text{if } \varepsilon_\lambda > \mu \,. \end{cases} \tag{16}$$

Replacing G in Eq. (15) by the expansion equation (14), one obtains once more the double sum over (λ,λ'). This sum is infinite and is usually calculated by truncating the single-particle basis. Instead of such an approximation procedure, the exact expression for $G(\mathbf{r}_1,\mathbf{r}_2,\varepsilon)$ is used in the coordinate representation method. Separating the angular variables in the usual way for the partial radial components $G_{ej}(r_1,r_2,\varepsilon)$, one has the exact expression

$$G_{ej}(r_1,r_2,\varepsilon) = y_1(r_<,\varepsilon)y_2(r_>,\varepsilon)/W[y_1,y_2] \,. \tag{17}$$

Here y_1 and y_2 are two independent solutions of the Schrödnger equation

$$[\varepsilon-(H_{\text{s.p.}})_{ej}]y(r,\varepsilon) = 0 \tag{18}$$

with different boundary conditions: $y_1(0,\varepsilon)=0$ and $y_2(\infty,\varepsilon)$ is finite. W in Eq. (17) stands for the Wronskian of the two solutions y_1 and y_2. Substituting Eq. (17) into Eq. (15) we obtain the exact expression for $\mathcal{A}$ which can be easily evaluated numerically. Eq. (17) into Eq. (15) we

obtain the exact expression for $\mathcal{A}$ which can be easily evaluated numerically.

When dealing with superfluid nuclei, in addition to the modification of the Green function G given by Eq. (14) into its superfluid analogue G_s, the two (Gorkov's) Green functions $F^{(1)}$, $F^{(2)}$ and the corresponding two new components of the transition density appear. Therefore the single Eq. (12) is transformed into a system of three equations [18]. The matrix form of this system has the same structure as Eq. (12):

$$\rho_\alpha = \mathcal{A}_{\alpha\beta}\mathcal{F}_{\beta\gamma}\rho_\gamma, \quad \gamma = 0,1,2 \ . \tag{19}$$

Here, for example, $\mathcal{A}_{\alpha\beta}$ are given by integrals of products of different combinations of the Green functions G_s, $F^{(1)}$, and $F^{(2)}$, instead of the single propagator in Eq. (13). The method outlined above cannot practically by applied in the complete form; however, a simplification can be used in this case [18]. The propagator $\mathcal{A}_{00}$ may be written

$$\mathcal{A}_{00} = (\mathcal{A}_{00} - \mathcal{A}_0) + \mathcal{A}_0 \ , \tag{20}$$

where $\mathcal{A}_0$ stands for the particle-hole propagator without taking into account the pairing effects. The idea of mixed (r,λ) representation is based on the simple fact that the pairing effects vanish rapidly when the single-particle energies are far from the Fermi energy ($|\varepsilon_\lambda - \mu| \gg \Delta$, $|\varepsilon_{\lambda'} - \mu| \gg \Delta$, $\Delta \sim 1$ MeV is the pairing gap). Therefore the term $(\mathcal{A}_{00} - \mathcal{A}_0)$ as well as other components $\mathcal{A}_{\alpha\beta}$ ($\alpha\beta \neq 00$) can be evaluated with high accuracy in the λ representation with the use of a truncated λ basis. The next term $\mathcal{A}_0$ in Eq. (20) should be calculated with the use of the coordinate representation as it is described above. Explicit formulas can be found in Ref. [18].

In principle, Eq. (19) should be solved in a self-consistent way, where the average nuclear field $U(r)$ is generated by the same effective interaction $\mathcal{F}(\mathbf{r},\mathbf{r}')$ which determines the transition densities. Then, for the multipolarity $J^\pi = 1^-$ one will automatically obtain the "ghost" solution with zero energy and the "transition density" $\rho^{1^-}_{\text{ghost}} = d\rho_0/dr$.

In fact, in Ref. [18] as well as in this section, a simplified version of the FFS theory was used employing the finite-range (Yukawa-type) effective force in combination with Woods-Saxon average field. One of the interaction parameters is chosen so as to put the ghost 1^--state energy to zero. This calculation scheme contains no free parameters.

The Woods-Saxon single-particle levels deviate, as a rule, by $\sim$1–2 MeV from the experimental ones. Such accuracy is insufficient for a consistent description of low-lying collective states. To some extent, an exception is presented by the energetically lowest 2^+_1 states, where most of the collectivity gathers, and therefore have low sensitivity to the details of the single-particle spectrum. The main goal of Ref. [18] was to confirm the surface nature of the first 2^+_1 states in superfluid nuclei. Thus the use of the simplified treatment was reasonable. For a quantitative description, such calculations should be considered preliminary. For the higher excitation states they are of less significance. They are more or less reasonable only for the cases when the state under consideration may be considered as a one-phonon excitation. The FFS densities for higher states are useful since the comparison between densities with the experimental and QPA results allow us to estimate the contribution of the one-phonon component.

V. RESULTS

The experimental spectra were analyzed up to an excitation energy of 3.3 MeV. Twenty-one levels were observed in this experiment and for most levels spin and parity assignments were confirmed or newly proposed. Table I lists excitation energies with spin and parity assignment for all the observed states [36]. The excitation energies and the $B(E\lambda)$ values of the low-lying states with different J^π obtained in the QPA are presented in the Table II along with corresponding FFS predictions and experimental results.

Transition charge densities have been extracted for many of these levels using a polynomial-Gaussian expansion. This expansion introduces more model dependence into the final densities than the Fourier-Bessel expansion of Ref. [25], but allows a reconstruction of the shape of the densities even though high-momentum-transfer data were unavailable. Errors presented thus represent the statistical uncertainty from the extracted cross sections but not the uncertainty due to lack of high-momentum-transfer data.

A. 2^+ states

In this experiment five 2^+ states have been observed. The form factors with DWBA fits for these 2^+ states are shown in Fig. 2. The calculations within the QPA predict more 2^+ states in the same energy region, but some of them have rather small $B(E2)$ values, and could not be observed in the present experiment. The transition

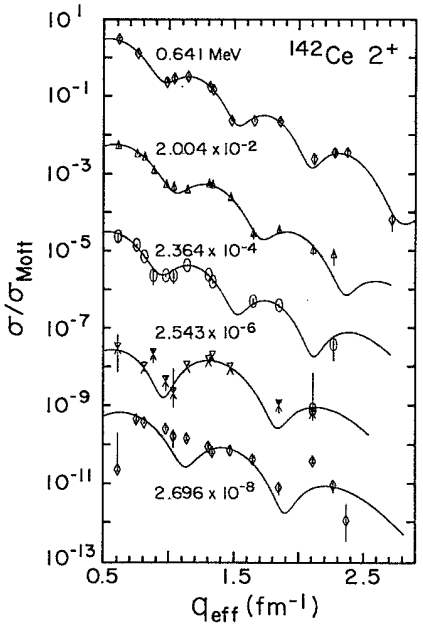

FIG. 2. Form factors for the 2^+ states at 0.6413, 2.004, 2.364, 2.543, and 2.696 MeV. The curves show the DWBA fits.

TABLE I. ^{142}Ce observed levels with J^π and $B(E\lambda)$ from this experiment.

E (MeV)	J^π	$B(E\lambda)$ (e^2 fm$^{2\lambda}$)	Comments
0.000	0^+		
0.641	2^+	$(4.61\pm0.21)\times10^3$	
1.219	4^+	$(2.45\pm0.52)\times10^6$	
1.536			Very weakly populated
1.653	3^-	$(2.33\pm0.12)\times10^5$	
1.742	5^-	$(6.0\pm2.2)\times10^6$	J^π previously known as 4^+ or 5^-
2.004	2^+	$(6.21\pm0.24)\times10^2$	
2.043	4^+	$(2.43\pm0.09)\times10^6$	J^π previously unknown
2.125	5^-	$(1.53\pm0.20)\times10^8$	J^π previously unknown
2.220	6^+	$(1.80\pm0.66)\times10^9$	Previously unknown state
2.279	4^+	$(2.29\pm0.39)\times10^5$	J^π previously unknown
2.364	2^+	$(4.80\pm0.39)\times10^2$	Previously known as $1^\pm$
2.543	2^+	$(5.10\pm0.47)\times10^1$	
2.590			
2.604			
2.696	2^+	$(5.0\pm1.8)\times10^1$	
2.742	1^-	$(1.20\pm0.28)\times10^0$	
2.767			
2.861			
3.000			
3.060	3^-	$(6.55\pm0.46)\times10^4$	J^π previously unknown
3.228	5^-	$(8.3\pm2.1)\times10^7$	J^π previously unknown

TABLE II. The excitation energies and the $B(E\lambda)$ values of the low-lying states with different J^π obtained in the QPA along with corresponding FFS predictions and experimental results.

		QPA		FFS		Experiment	
J^π	ν	E_x (MeV)	$B(E\lambda)$(e^2 fm$^{2\lambda}$)	E_x (MeV)	$B(E\lambda)$(e^2 fm$^{2\lambda}$)	E_x (MeV)	$B(E\lambda)$(e^2 fm$^{2\lambda}$)
1^-	1	2.51	2.52×10^{-2}			2.742	$(1.20\pm0.28)\times10^0$
	2	4.71	1.19×10^{-2}				
2^+	1	0.59	4.16×10^3	0.664	3.00×10^3	0.641	$(4.61\pm0.21)\times10^3$
	2	1.62	1.05×10^0			1.536	
	3	2.09	5.47×10^2	1.658	3.19×10^2	2.004	$(6.21\pm0.24)\times10^2$
	4	2.22	1.69×10^1	1.917	7.33×10^1	2.543	$(5.10\pm0.47)\times10^1$
	5	2.35	6.76×10^{-2}				
	6	2.57	2.31×10^1			2.696	$(5.0\pm1.8)\times10^1$
	7	3.14	4.47×10^2	2.710	7.61 ± 10^1	2.364	$(4.80\pm0.39)\times10^2$
	8	3.32	1.21×10^2				
3^-	1	1.64	1.27×10^5	1.578	2.34×10^5	1.653	$(2.33\pm0.12)\times10^5$
	2	3.24	4.87×10^3	3.735		3.060	
	3	3.34	5.92×10^4	3.735	1.05×10^4	3.060	$(6.55\pm0.46)\times10^4$
	4	3.53	4.36×10^3				
4^+	1	1.33	3.23×10^6	1.306	1.83×10^6	1.219	$(2.45\pm0.52)\times10^6$
	2	1.95	2.16×10^6	1.672	9.47×10^5	2.043	$(2.43\pm0.09)\times10^6$
	3	2.14	2.14×10^5			2.279	$(2.29\pm0.39)\times10^5$
	4	2.26	1.66×10^5			2.279	
	5	2.31	4.31×10^1				
	6	2.38	2.77×10^4				
	7	3.08	1.02×10^6				
	8	3.31	2.41×10^4				
	9	3.66	1.19×10^5				
5^-	1	2.15	1.28×10^8	2.539	7.20×10^7	2.125	$(1.53\pm0.20)\times10^8$
	2	3.10	8.76×10^7			3.228	$(8.3\pm2.1)\times10^7$
	3	3.29	2.08×10^6				
	4	3.49	3.99×10^6				
6^+	1	1.83	5.63×10^8				
	2	2.22	2.73×10^9	1.795	2.17×10^9	2.220	$(1.80\pm0.66)\times10^9$
	3	2.28	2.40×10^6				
	4	2.70	8.25×10^6				
	5	3.38	2.43×10^7				

charge densities of these states are presented in Fig. 3. In this (and the following figures) we also present for comparison the densities obtained in the QPA calculations by the solid curves and in the FFS theory calculations by the dashed curves.

The first 2^+ state, at an excitation energy of $E_x = 0.6413$ MeV, has a strong surface peak with the maximum at 5.8 fm. This is a very collective state and both theories reproduce the position and the amplitude of the exterior peak, although they overestimate the amplitude of the peak in the interior. There are several reasons

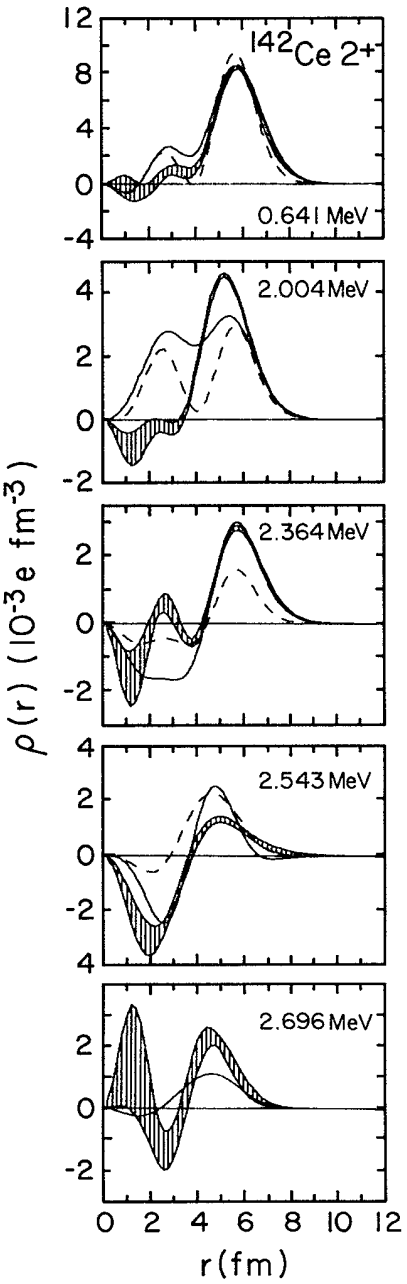

FIG. 3. Transition charge densities for the 2^+ states at 0.6413, 2.004, 2.364, 2.543, and 2.696 MeV. The solid curves are the QPA calculations while the dashed curves are the FFS predictions.

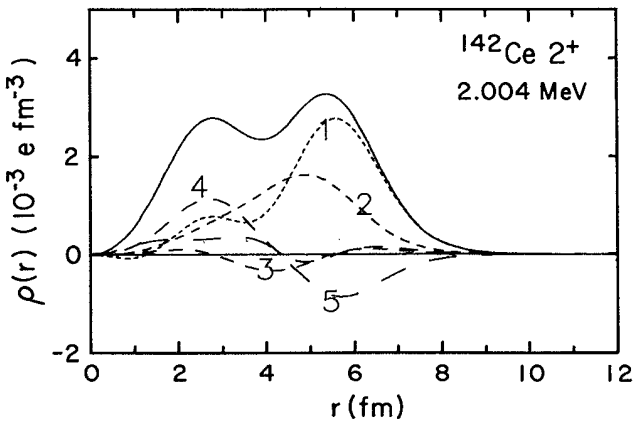

FIG. 4. Transition charge densities predicted in QPA for the 2.004-MeV state decomposed into the first, second, third, fourth, and fifth one-phonon 2^+ configurations.

for the poorer description of the interior behavior of densities, which are more sensitive to details of calculations than is the surface behavior. The surface peaks for collective states are produced as a result of coherent interference of a large number of two-quasiparticle components, while in the interior the interference is mainly destructive and the results may depend strongly on the separate contribution of each component. One of the most important sources of inaccuracy in the calculated densities in both approaches are the uncertainties in the single-particle level scheme.

The second 2^+ state, known from the Nuclear Data Sheets [36] to be at $E_x = 1.536$ MeV, is very weakly populated in the present experiment. This state has a strong two-phonon component, since the $E2$ transition from this state to the 2_1^+ has the same value as from the 2_1^+ state to the ground state. This is confirmed by the QPA calculations, since for the second 2^+ state at $E_x = 1.62$ MeV, a

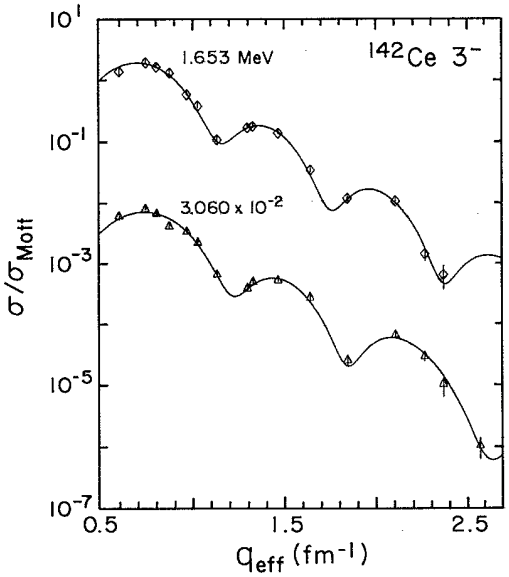

FIG. 5. Form factors for the 3^- states at 1.653 and 3.060 MeV.

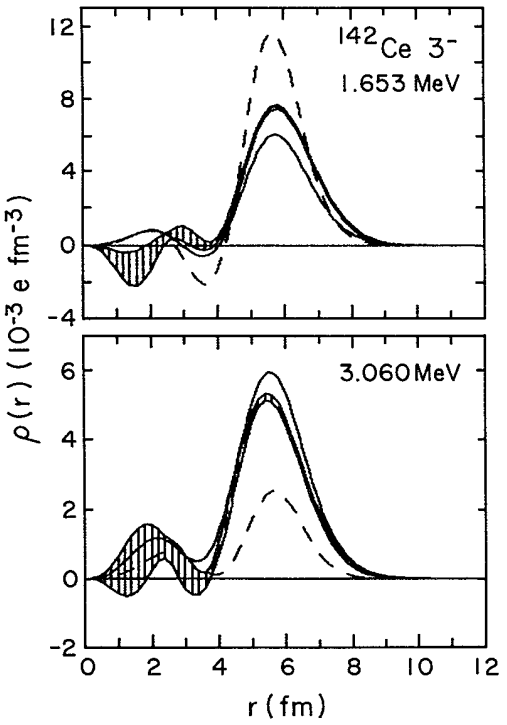

FIG. 6. Transition charge densities for the 3^- states at 1.653 and 3.060 MeV. The solid curve in 3.060 MeV represents the sum of the calculated densities (QPA) of the 3.24- and 3.34-MeV states.

49% contribution comes from the two-phonon configuration $[2_1^+ \otimes 2_1^+]_{2+}$ and the difference between the $2_2^+ \rightarrow 2_1^+$ and $2_1^+ \rightarrow 0_{g.s.}^+$ transitions is only a few percent, while the $2_2^+ \rightarrow 0_{g.s.}^+$ transition is much weaker. For this reason, the second 2^+ state is not expected to be strongly excited by electron scattering.

The second observed 2^+ state has an excitation energy of 2.004 MeV and the exterior peak of its density has the maximum around 5.2 fm. Within the QPA, the state at $E_x = 2.09$ MeV has a very complex structure: the main component (35%) arises from the second one-phonon 2^+ configuration, though the first, fourth, and fifth one-phonon 2^+ configurations give a visible contribution to the density of this state. This is shown in Fig. 4, in which these contributions are presented. The interference between these configurations causes the shift of the exterior maximum to the 5.4 fm and the strong interior peak is the result of coherent interference inside the nucleus. This interior peak is not seen in the experiment although it is also predicted by the FFS calculations. It should be noted that in such cases with a very complicated structure of the excited states, the FFS theory within the one-phonon approximation should be considered only in a qualitative way.

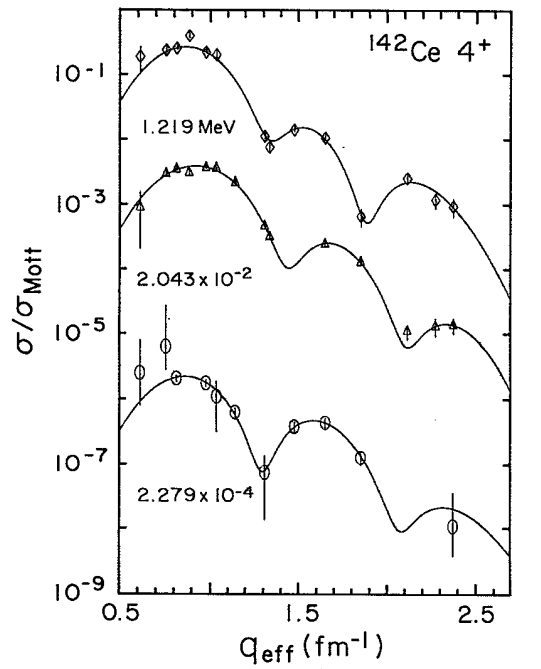

FIG. 7. Form factors for the 4^+ state sat 1.219, 2.043, and 2.279 MeV.

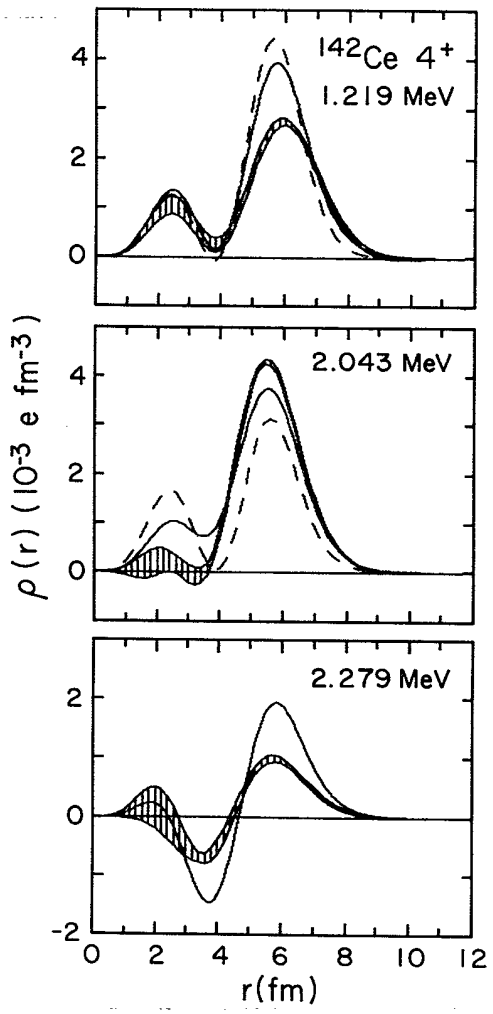

FIG. 8. Transition charge densities for the 4^+ states at 1.219, 2.043, and 2.279 MeV. The solid curve corresponding to the 2.279-MeV level is the sum of two neighboring states at $E_x = 2.14$ and 2.26 MeV calculated within the QPA.

The third 2^+ state detected in this experiment at $E_x=2.364$ MeV has a spin and parity which is given in Nuclear Data Sheets [36] as $J^\pi=1^\pm$, but the form factor for this states fits $J^\pi=2^+$ very well. The density of this state has as strong a surface peak at 5.8 fm as for the 2_1^+ state, indicating that this state is essentially collective. The seventh 2^+ state in the QPA with $E_x=3.14$ MeV (approximately 63%, comes from the fifth 2^+ one-phonon configuration) and the fourth 2^+ state in the FFS calculations with $E_x=2.710$ MeV correspond to this state. Although the 2.364-MeV state is located in the calculations at a higher energy, this state, like the first 2^+ state, is rather collective. The fifth 2^+ one-phonon configuration is located in the QPA calculations at $E_x=3.41$ MeV, but due to the interaction with complex configurations it is fragmented and a strong fragment of it is shifted to lower energies. It is possible that if a larger number of complex configurations are included in the calculation, it will shift the excitation energy closer to the experimental value. However, the uncertainties in the single-particle level's position, mentioned above, can be another reason for the high value of E_x for this state.

The fourth and fifth detected 2^+ states are rather weak and both exhibit a great deal of structure in the nuclear interior; that is reproduced by the theoretical calculations, together with the excitation energies. In the QPA the fourth and sixth excited 2^+states with $E_x=2.22$ and 2.57 MeV, respectively, constructed from the noncollective second, third, and fourth 2^+ one-phonon configurations are the corresponding theoretical densities.

It is interesting to compare results for the low-lying 2^+ states obtained here for ^{142}Ce with those for ^{142}Nd published in Ref. [12]. Two additional neutrons above the closed shell $N=82$ strongly enhance the interplay between different components in the wave functions of excited states in Eq. (2). The matrix elements for interaction between one- and two-phonon configurations $\overline{U}^{L''i''}_{L'i'}$(Li) are larger for nonmagic ^{142}Ce than for half-magic nucleus ^{142}Nd. As a result, we obtain a rather complex structure of many low-lying states in ^{142}Ce while the structure of low-lying states in ^{142}Nd is determined mainly by only one component of the wave function [12] with the contribution of more than 90% for each state.

B. 3^- states

Two 3^- states were observed in the present experiment. The form factors and transition charge densities for these 3^- states are shown in Figs. 5 and 6, respectively. The first state has an excitation energy of 1.653 MeV and the maximum of its density is located at 5.8 fm; the

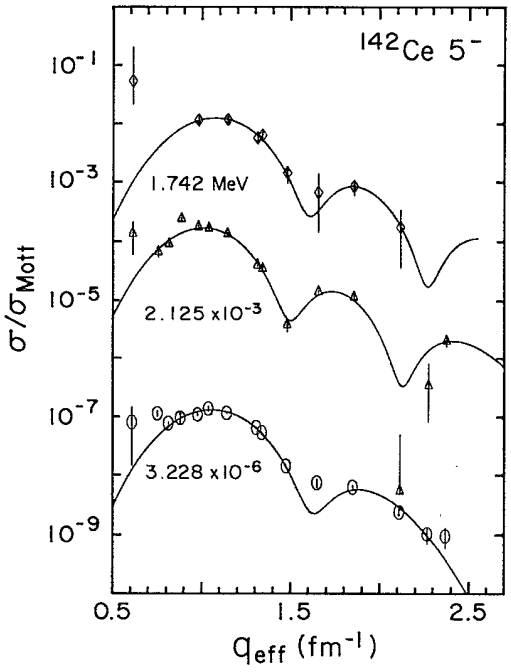

FIG. 9. Form factors for the 5^- states at 1.742, 2.125, and 3.228 MeV.

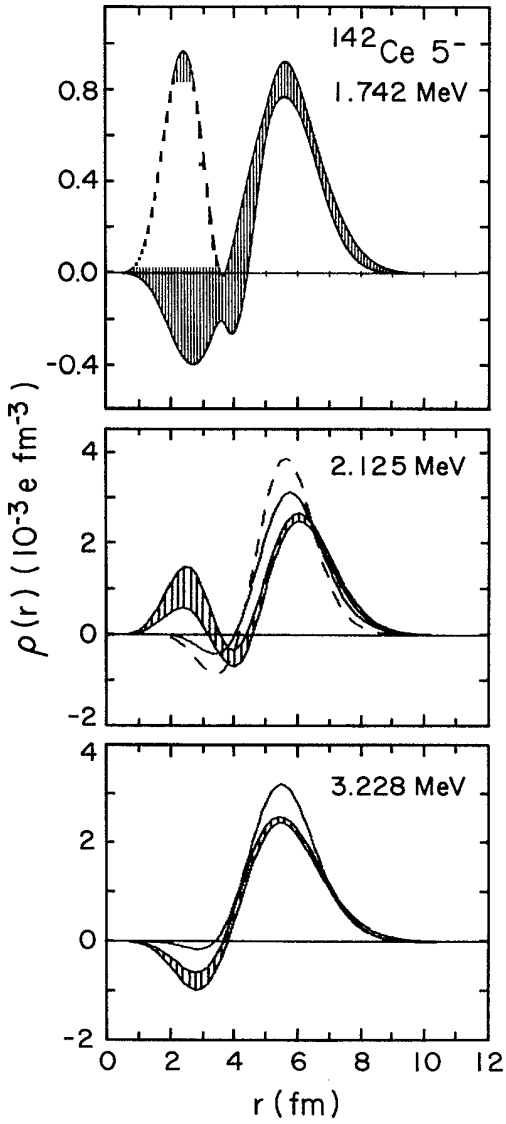

FIG. 10. Transition charge densities for the 5^- states at 1.742, 2.125, and 3.228 MeV.

maximum of the second state at $E_x=3.060$ MeV is shifted to the interior and located approximately at 5.4 fm. In the QPA three 3^- states near 3.0 MeV are predicted. The strength of the collective first 3^- one-phonon term is distributed mainly between the first (55%) and third (32%) 3^- states in QPA with $E_x=1.64$ and 3.34 MeV, respectively. The main contribution (86%) to the second 3^- state in QPA with $E_x=3.24$ MeV comes from the noncollective second 3^- one-phonon term. The experimental position of the density maximum of the 3_1^- state is well reproduced by the theory. To compare the density of the 3_2^- we plot in Fig. 6 the sum of the calculated densities of stats which are located very close together: the second at $E_x=3.24$ MeV and the third $E_x=3.34$ MeV in QPA. The interference between the noncollective second 3^- state ($E_x=3.24$ MeV) in QPA with a density maximum at 4.9 fm and the collective third 3^- state ($E_x=3.34$ MeV) in QPA with a maximum at 5.7 fm produces a resulting density with its maximum at 5.5 fm, close to the experimental value. In the FFS calculations the shape and peak position for both states are well reproduced. However, the 3_1^- state is too collective, while the collectivity of the 3_2^- state is underestimated.

C. 4^+ states

The form factors and the transition charge densities for the 4^+ states are presented in Figs. 7 and 8, respectively. The first 4^+ state is located at the excitation energy 1.219 MeV and the maximum of its density is near 5.9 fm. Both theories overestimate slightly the collectivity of this state, but the shape of density is well reproduced. In the QPA the main contribution (50%) to the structure of this state comes from the first one-phonon configuration, though a visible contribution (25%) is coming from two-phonon configuration $[2_1^+\otimes 2_1^+]_{4^+}$.

The second 4^+ state, with an experimental energy of 2.043 MeV, has a more complex structure. Three main configurations (the first and second one-phonon configurations and the two-phonon configuration $[2_1^+\otimes 2_1^+]_{4^+}$) give approximately the same contribution (about 22% each) to the structure of this state. For this reason, the FFS density for the 4_2^+ state in Fig. 8 can be considered only qualitatively. The interplay between the first and second one-phonon configurations explains the shift of maximum of the 4_2^+ state density to the interior compared to the 4_1^+ density (in the experiment is shifted from 5.9 to 5.4 fm and in the QPA calculations from 5.7 to 5.5 fm).

The structure of the higher 4^+ states is even more complex. Many one-phonon configurations contribute to these states. For a comparison with the density of the observed third 4^+ state at $E_x=2.279$ MeV we plot in Fig. 8 the sum of two close-lying states at $E_x=2.14$ MeV and $E_x=2.26$ MeV calculated within the QPA. The density of this state again exhibits the surface maximum, but for this state this is not an indication of the state's collectivity but the result of a strong interplay between different configurations in the wave function of excited state.

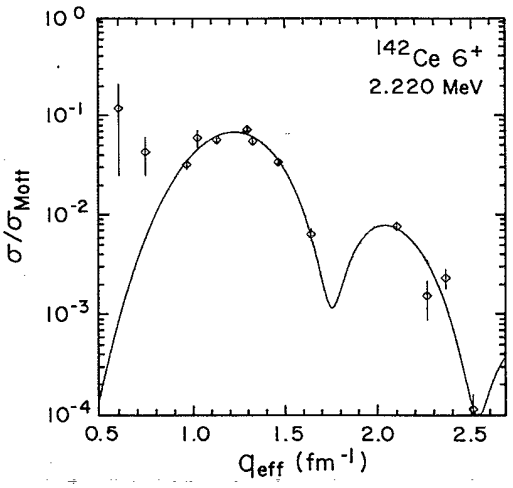

FIG. 11. Form factor for 6^+ state at 2.220 MeV.

D. 5^- states

Three 5^- states are observed in this experiment. Figures 9 and 10 show the form factors and transition charge densities, respectively. The first state, with an excitation energy of 1.742 MeV, was previously reported as a 4^+ or 5^- state [36]. The form factor obtained in this experiment does not fit well to 4^+, but is well described by an assumption of $J^\pi=5^-$. No calculation within QPA or FFS predicts any state corresponding to this level.

A collective 5^- state with the peak of its density near 6.0 fm (Fig. 10) has been observed at the excitation energy $E_x=2.125$ MeV. In both theories the first 5^- state has E_x close to the experimental value, although the structure of this state is different in the QPA and the FFS. In the one-phonon approximation of the FFS theory this is a one-phonon state, while the QPA predicts a large contribution (47%) to the structure of this state coming from the two-phonon configuration $[2_1^+\otimes 3_1^-]_{5^-}$. Since the shape of the density is determined mainly by the one-phonon configurations, the resulting density in the QPA has the same features as in the FFS calculations.

The surface peak of the next 5^- state at $E_x=3.228$ MeV is located around 5.5 fm. This state does not appear

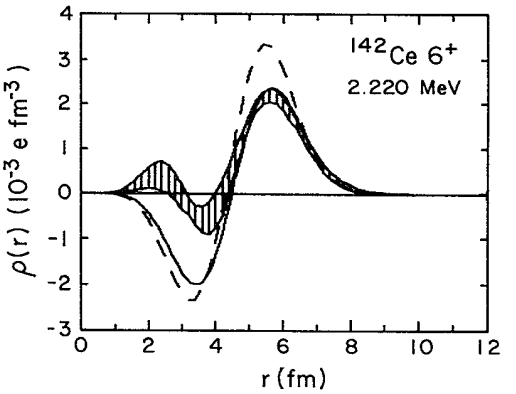

FIG. 12. Transition charge density for the 6^+ state at 2.220 MeV.

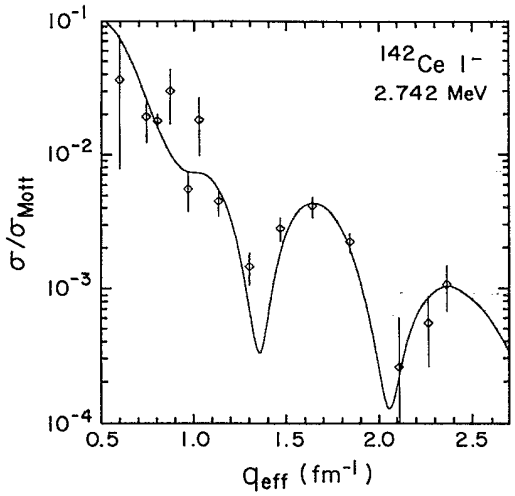

FIG. 13. Form factor for the 1^- state at 2.742 MeV.

in the FFS calculations and the reason is clear if we examine the structure of the second 5^- state (E_x=3.10 MeV) in the QPA. The main one-phonon component in the structure of this state is the same as for the first 5^- state (E_x=2.15 MeV) in the QPA, however, due to the interaction with complex configurations, the strength of the first one-phonon component is distributed between these two 5^- states. This also explains why the shapes of densities of these states are quite similar—the shift of the surface maximum from 5.7 fm of the first 5^- state (E_x=2.15 MeV) to 5.5 fm of the second 5^- state (E_x=3.10 MeV) in QPA is caused by the weak contribution coming from the second one-phonon configuration to the structure of the second 5^- state in QPA.

E. 6^+ states

We have detected a state at E_x=2.220 MeV which has not been previously reported. Its form factors (Fig. 11) is well described by an assumption of $J^\pi=6^+$. The extracted density (Fig. 12) has its maximum at 5.6 fm. Both theories predict a 6^+ state in this energy region with a shape rather similar to the observed density.

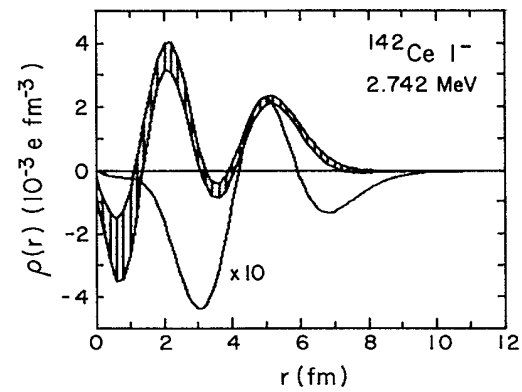

FIG. 14. Transition charge density for the 1^- state at 2.742 MeV. The solid curve is the QPA prediction multiplied by ten.

F. 1^- states

The lowest-lying 1^- state detected in the experiment (Fig. 13) has the excitation energy 2.742 MeV and a rather special shape of its transition density, presented in Fig. 14. If we turn to the QPA calculations, the first 1^- one-phonon configuration is located at E_x=7.33 MeV, while the lowest 1^- configuration at E_x=4.08 MeV has the two-phonon origin $[2_1^+\otimes 3_1^-]_{1^-}$. This two-phonon $[2_1^+\otimes 3_1^-]_{1^-}$ configuration strongly interacts with three-phonon terms in the wave function of excited states. Due to this interaction 71% of its strength is pushed down to the excitation energy 2.51 MeV. The contribution of the one-phonon configurations to the first 1^- state is less than 1%, the rest (28%) comes from the three-phonon terms of the wave function (the largest contribution is from the configuration $[[2_1^+\otimes 3_1^-]_3\otimes 2_1^+]_{1^-}$-about 25%). In the present calculations the "ghost" 1^- state is excluded in the one-phonon approximation only, but the corrections due to the more complex configurations taken into account will be small. The shape of the density proves to be in qualitative agreement with the experimental one, while the $B(E1)$ value and the amplitude of peaks are strongly underestimated by theory. The reason for such large disagreement is not clear. The oscillating shape of 1^- state was also observed in ^{208}Pb [37].

VI. SUMMARY AND CONCLUSIONS

In this experiment, electron scattering cross sections for the low-lying states of ^{142}Ce have been measured for excitation energies up to 3.3 MeV. The excellent energy resolution made it possible to separate the form factors of 21 low-lying states. For 15 of these states accurate transition charge densities were extracted by means of DWBA analysis using polynomial-Gauss model to model the transition density. For most levels, spin and parity assignments were confirmed or newly proposed. A previously unreported level has been found with an excitation energy of 2.220 MeV and $J^\pi=6^+$. The diversity of the data, with multipolarities ranging from 1^- to 6^+, allows a systematic investigation of the modes of excitation of these low-lying states.

In this work, special attention has been given to the interplay between single-particle and collective degrees of freedom. To this end, the experimental results were compared with calculations in the framework of the quasiparticle-phonon approach and finite Fermi system theory. In this nonmagic nucleus, the interaction between one-, two-, and three-phonon components is rather strong. The largest matrix elements of interaction are between collective 2_1^+, 3_1^-, 4_1^+ one-phonon components and two-phonon components constructed from these collective phonons. Due to this interaction, pure one-, two-, and three-phonon states which we would have if the interaction between these components is not taken into account, are fragmented over the states and the excitation energies of collective states are shifted by more than 1 MeV to lower energies where they are detected experi-

mentally. The comparison of ^{142}Ce with ^{142}Nd indicates that the two additional neutrons above the closed shell $N=82$ strongly increase the interplay between different components in the wave functions of excited states.

In general, the agreement between the experimentally extracted transition charge densities and theoretical calculations is quite good. The poorer description of the interior behavior of densities can be attributed to the destructive nature of the interference. For the second and higher-lying states, the FFS theory within a "one-phonon approximation" is reasonable only for the cases when the state under consideration is manly the one-phonon one. A more refined self-consistent calculation in terms of FFS theory is in progress now, and we hope that this will provide a more consistent description of the low-lying collective states.

ACKNOWLEDGMENTS

We would like to thank the staff at the MIT-Bates Linear Accelerator Center for their efforts in providing us with the high quality beams and support necessary for this experiment. We would like to thank Professor F. Iachello for valuable discussions. One of us (V.Yu.P.) would like to thank Dr. M. Grinberg, Dr. D. Karadjov, Dr. Ch. Stoyanov, Dr. A. I. Vdovin, and Dr. V. V. Voronov for fruitful discussions. One of us (W. K.) would like to thank JINR and Kurchatov Institute of Atomic Energy for their support and hospitability during the visit. This work was supported, in part, by the Department of Energy through Contract No. DE-AS02-76ER10338 and the National Science Foundation through Grant No. NSF PHY 86-10493.

*Present address: Department of Physics, Catholic University of America, Washington, D.C. 20064.

†Present address: Nuclear Physics Laboratory, University of Colorado, Boulder, CO 80309-0390.

[1] J. Lichtenstadt, J. H. Heisenberg, C. N. Papanicolas, and C. P. Sargent, Phys. Rev. C **20**, 497 (1979).

[2] G. F. Bertsch and S. F. Tsai, Phys. Lett. **50B**, 319 (1974); Phys. Rep. **C18**, 125 (1975).

[3] V. A. Khodel, Zh. Eksp. Teor. Fiz. **16**, 410 (1972) [Sov. Phys. JETP Lett. **16**, 291 (1972)]; **18**, 126 (1973) [**18**, 72 (1973)]; Yad. Fiz. **19**, 792 (1974) [Sov. J. Nucl. Phys. **19**, 404 (1974)].

[4] S. A. Fayans, V. A. Khodel, and E. E. Saperstein, Nucl. Phys. **A317**, 424 (1979).

[5] V. A. Khodel and E. E. Saperstein, Nucl. Phys. **A348**, 261 (1980).

[6] R. Neuhausen, J. W. Lightbody, Jr., S. P. Fivozinsky, and S. Penner, Nucl. Phys. **A263**, 249 (1976).

[7] S. F. Tsai and G. F. Bertsch, Phys. Lett. **59B**, 425 (1975).

[8] C. N. Papanicolas, J. Heisenberg, J. Lichtenstadt, J. S. McCarthy, D. Goutte, J. M. Cavedon, B. Frois, M. Huet, P. Leconte, and I. Sick, Phys. Rev. Lett. **52**, 247 (1984).

[9] O. Schwentker, J. Dawson, J. Robb, J. Heisenberg, J. Lichtenstadt, C. N. Papanicolas, J. Wise, J. S. McCarthy, L. T. van der Bijl, and H. P. Blok, Phys. Rev. Lett. **50**, 15 (1983).

[10] X. H. Phan, H. G. Andresen, L. S. Cardman, J. M. Cavedon, J. C. Clemens, B. Frois, M. Girod, D. Gogny, D. Goutte, B. Grammaticos, R. Hofmann, M. Huet, P. Leconte, S. K. Platchkov, I. Sick, and S. E. Willamson, Phys. Rev. C **38**, 1173 (1988).

[11] V. Meot, Ph.D. thesis, De L'Universite Paris VII, 1987.

[12] R. K. J. Sandor, H. P. Blok, U. Garg, M. N. Harakeh, C. W. de Jager, V. Yu. Ponomarev, A. I. Vdovin, and H. de Vries, Phys. Lett. B **233**, 54 (1989).

[13] R. K. J. Sandor, Ph.D. thesis, Vrije Univeristeit Te Amsterdam, 1991.

[14] V. G. Soloviev, *Theory of Complex Nuclei* (Pergamon, Oxford, 1976).

[15] A. I. Vdovin and V. G. Soloviev, Yad. Fiz. **14**, 237 (1983) [Sov. J. Part. Nucl. **14**, 99 (1983)]

[16] V. V. Voronov and V. G. Soloviev, Yad. Fiz. **14**, 1380 (1983) [Sov. J. Part. Nucl. **14**, 583 (1983)].

[17] V. G. Soloviev, Progr. Part. Nucl. Phys. **19**, 107 (1987).

[18] A. P. Platonov and E. E. Saperstein, Nucl. Phys. **A486**, 63 (1988).

[19] W. Bertozzi, M. V. Hynes, C. P. Sargent, W. Turchinetz, and C. Williamson, Nucl. Instrum. Methods **162**, 211 (1979).

[20] W. Bertozzi, M. V. Hynes, C. P. Sargent, C. Cresswell, P. C. Dunn, A. Hirsh, M. Seitch, B. Norum, F. N. Rad, and T. Sasanuma, Nucl. Instrum. Methods **141**, 457 (1977).

[21] F. W. Hersman, Ph.D. thesis, MIT, 1982.

[22] J. J. Kelly, C. E. Hyde-Wright, and F. W. Hersman, ALLFIT computer code, unpublished.

[23] J. Bergstrom, in *MIT 1967 Summer Study, Medium Energy Nuclear Physics with Electron Accelerators* (MIT, Cambridge Massachusetts, 1967), p. 251.

[24] R. Engfer, H. Schneuwly, J. L. Vuilleumier, H. K. Walter, and A. Zehnder, At. Data Nucl. Data Tables **14**, 509 (1974).

[25] J. Heisenberg, Adv. Nucl. Phys. **12**, 61 (1981).

[26] V. Yu. Ponomarev, O. Stoyanova, and Ch. Stoyanova, Report No. JINR, P4-81-704, Dubna, 1981.

[27] V. G. Soloviev, Ch. Stoyanov, and R. Nikolaeva, Izv. Akad. Nauk SSSR Ser. Fiz. **47**, 2082 (1983) [Izv. Akad. NAUK SSSR Physical Series **47** (11), 1 (1983)].

[28] H. C. Lee, Chalk River Nuclear Laboratories, Report No. AECL-4839, Chalk River, Ontario, 1975; J. H. Heisenberg and H. P. Blok, Annu. Rev. Nucl. Part. Sci. **33**, 569 (1983).

[29] G. G. Simon, C. Schmitt, F. Borkowski, and F. W. Walther, Nucl. Phys. **A333**, 381 (1980).

[30] J. B. A. M. Lanen, NIKHEFK-K, Amsterdam, private communication.

[31] V. Yu. Ponomarev, V. G. Soloviev, Ch. Stoyanov, and A. I. Vdovin, Nucl. Phys. **A323**, 446 (1979).

[32] V. A. Khodel, A. P. Platonov, and E. E. Saperstein, J. Phys. G **8**, 967 (1982).

[33] S. Shlomo and G. F. Berstsch, Nucl. Phys. **A243**, 507 (1975).

[34] E. E. Saperstein, S. V. Tolokonnikov, and S. A. Fayans, Report No. IAE-2571 1975.

[35] V. A. Khodel and E. E. Saperstein, Phys. Rep. **92**, 183 (1982).

[36] L. K. Peker, Nucl. Data Sheets **43**, 579 (1984).

[37] J. Heisenberg and H. P. Blok, Annu. Rev. Nucl. Part Sci. **33**, 569 (1983).